AIAA JOURNAL
Vol. 42, No. 2, February 2004

Essentially Nonoscillatory Finite Volume Scheme for Electromagnetic Scattering by Thin Dielectric Coatings

A. Chatterjee* and A. Shrimal†
Indian Institute of Technology, Bombay, Mumbai 400 076, India

A high-resolution method in the form of the essentially nonoscillatory scheme is used to solve Maxwell's equations in the time domain in a finite volume time-domain framework. This formulation is used to predict the radar cross section of perfectly conducting scatterers coated with a very thin layer of lossy or nonlossy dielectric. A direct formulation is used in which the Maxwell's equations are solved in freespace, as well as in the dielectric layer, without any special treatment. Traditionally, the prediction of scattering from very thin dielectric layers without special treatment is known to incur numerical instabilities. Results are presented for the sphere and cone sphere with perfectly conducting surfaces coated with a very thin layer of lossy and nonlossy dielectric.

Nomenclature

a_1	=	radius of coated sphere
a_2	=	radius of uncoated sphere
$\boldsymbol{B}$	=	magnetic induction
B_x, B_y, B_z	=	components of magnetic induction
$\boldsymbol{D}$	=	electric field displacement
D_x, D_y, D_z	=	components of electric field displacement
$\boldsymbol{E}$	=	electric field vector
E_x, E_y, E_z	=	components of electric field vector
$\boldsymbol{F}$	=	flux vector
$\boldsymbol{f}, \boldsymbol{g}, \boldsymbol{h}$	=	flux vectors in Cartesian coordinate directions
$\boldsymbol{H}$	=	magnetic field vector
H_x, H_y, H_z	=	components of magnetic field vector
$\boldsymbol{J}_i$	=	impressed current density vector
j	=	imaginary unit
k	=	incident electromagnetic wave number
$\hat{\boldsymbol{n}}$	=	unit surface normal
S	=	stencil
$\boldsymbol{S}$	=	entire source term contribution from incident field
$\mathcal{S}$	=	surface domain of integration
$\boldsymbol{s}$	=	source term vector
t	=	thickness of dielectric coating
$\boldsymbol{u}$	=	state vector
$\mathcal{V}$	=	volume domain of integration
x, y, z	=	Cartesian coordinates
ε	=	electric permittivity
ε_r	=	complex relative permittivity
λ	=	wavelength
μ	=	magnetic permeability
μ_r	=	complex relative permeability
ρ	=	equivalent magnetic resistivity
σ	=	electrical conductivity
ω	=	angular frequency

Subscripts

j	=	cell index
m	=	cell face
num	=	numerical flux contribution
t	=	partial derivative with respect to t
x, y, z	=	partial derivative with respect to x, y, z

Superscripts

i	=	incident field
s	=	scattered field
$'$	=	real part
$''$	=	imaginary part
$\tilde{}$	=	volume average
$\bar{}$	=	numerical flux function

Received 27 January 2003; revision received 3 September 2003; accepted for publication 26 September 2003.

*Assistant Professor, Department of Aerospace Engineering; avijit@aero.iitb.ac.in.
†Graduate Student, Department of Aerospace Engineering; anuj@aero.iitb.ac.in.

Introduction

In recent times, there has been an increasing trend toward solving Maxwell's equations in the time domain by the use of characteristic-based finite volume time-domain (FVTD) techniques.[1–4] The main advantage of FVTD techniques lies in their ability to handle (in principle) complex geometries with different material properties for the whole range of frequencies within a unified framework. The main disadvantage is the requirement of large computing resources, especially at large electrical sizes. The time-domain Maxwell's equations may be posed as a set of hyperbolic conservation laws when written in total field form. Characteristic-based numerical techniques are well known to model hyperbolic conservation laws accurately, especially when field discontinuities are involved.

In aircraft structures, there is an increasing tendency to use composite materials due to structural considerations. Low observability requirements often require aircraft to be coated with radar-absorbing materials (RAM) to absorb electromagnetic waves. Aircraft also incorporate radar-transparent structures or partially transparent structures for radome construction that are often combined with background absorbers for low-observability requirements. Thus, radar cross section predictions involving radar absorbing materials and structures become a crucial element of computational electromagnetics capability.

The algorithm used to solve the time-domain Maxwell's equations in the present study is based on the essentially nonoscillatory (ENO) scheme,[5,6] originally developed to solve hyperbolic conservation laws in the form of the Euler equations of gasdynamics. The ENO scheme has been very successfully applied to the numerical solution of the Euler and Navier–Stokes equations.[7] The ENO scheme has the dual capacity for higher-order accuracy and nonoscillatory resolution of discontinuities in the solution. Thus, the ENO scheme is particularly attractive for the resolution of a gasdynamic flowfield containing both strong shocks and rich smooth region structures. The ENO methodology has also been successfully used in more varied fields, including relativistic hydrodynamics and

semiconductor device simulation.[7] In the present study, we extend this methodology to the numerical solution of the Maxwell's equations in the time domain. Given the inherent features of the ENO methodology (uniformly high-order accurate, but ENO interpolation for piecewise smooth function), a time-domain Maxwell solver based on the ENO methodology could be an attractive choice with which to model computational electromagnetics (CEM) problems involving rapid changes in material properties, presence of resistance and material cards, presence of cracks and sharp corners, and, in general, in dealing with field discontinuities.

In the present work, we extend the ENO methodology to solve for electromagnetic scattering from canonical shapes having perfectly conducting surfaces coated with a very thin layer of lossy and nonlossy dielectric. Such problems involve resolution of a discontinuous change in material properties at the dielectric–freespace interface, in addition to resolution of the very thin dielectric layer. The formulation is direct in the sense that Maxwell's equations are solved in freespace, as well as in the dielectric layer, in a unified framework. The smaller wavelengths in the dielectric layer imply finer discretization inside the layer compared to that prevailing in freespace, leading to increased computational costs. This increase is limited if the dielectric layer is very thin. Direct formulations in the context of the frequency domain (integral equations formulation) require special treatment to deal with numerical instabilities incurred while dealing with very thin dielectric layers.[8] The alternative approach is the approximation of the effect of the dielectric layer by the so-called impedance boundary condition imposed on the surface of the scatterer and solution of the associated scattering problem.

Governing Equations

Maxwell's curl equations in the differential form incorporating lossy materials (electric and magnetic) can be expressed as

$$\frac{\partial \boldsymbol{B}}{\partial t} = -\nabla \times \boldsymbol{E} - \rho \boldsymbol{H} \tag{1}$$

$$\frac{\partial \boldsymbol{D}}{\partial t} = \nabla \times \boldsymbol{H} - \boldsymbol{J}_i - \sigma \boldsymbol{E} \tag{2}$$

The loss mechanisms are provided by σ, the effective electrical conductivity, and ρ, the equivalent magnetic resistivity. Also,

$$\boldsymbol{D} = \varepsilon' \boldsymbol{E} \tag{3}$$

$$\boldsymbol{B} = \mu' \boldsymbol{H} \tag{4}$$

$$\sigma = \omega \varepsilon'' \tag{5}$$

$$\rho = \omega \mu'' \tag{6}$$

where $\varepsilon''/\varepsilon'$ is the electric loss tangent, μ''/μ' the magnetic loss tangent (both zero for perfect dielectrics), and ω the angular frequency.

Whereas operations are performed in the frequency domain, it is standard practice to express the permittivity and permeability in lossy materials as a complex relative permittivity ε_r and complex relative permeability μ_r:

$$\varepsilon_r = \varepsilon' - j\varepsilon'' \tag{7}$$

$$\mu_r = \mu' - j\mu'' \tag{8}$$

Maxwell's equations can be recast in a conservative total field form as

$$\boldsymbol{u}_t + \boldsymbol{f}(\boldsymbol{u})_x + \boldsymbol{g}(\boldsymbol{u})_y + \boldsymbol{h}(\boldsymbol{u})_z = \boldsymbol{s} \tag{9}$$

where

$$\boldsymbol{u} = \begin{pmatrix} B_x \\ B_y \\ B_z \\ D_x \\ D_y \\ D_z \end{pmatrix}, \quad \boldsymbol{f} = \begin{pmatrix} 0 \\ -D_z/\varepsilon' \\ D_y/\varepsilon' \\ 0 \\ B_z/\mu' \\ -B_y/\mu' \end{pmatrix}, \quad \boldsymbol{g} = \begin{pmatrix} D_z/\varepsilon' \\ 0 \\ -D_x/\varepsilon' \\ -B_z/\mu' \\ 0 \\ B_x/\mu' \end{pmatrix}$$

$$\boldsymbol{h} = \begin{pmatrix} -D_y/\varepsilon' \\ D_x/\varepsilon' \\ 0 \\ B_y/\mu' \\ -B_x/\mu' \\ 0 \end{pmatrix}, \quad \boldsymbol{s} = \begin{pmatrix} -\rho H_x \\ -\rho H_y \\ -\rho H_z \\ -J_{ix} - \sigma E_x \\ -J_{iy} - \sigma E_y \\ -J_{iz} - \sigma E_z \end{pmatrix} \tag{10}$$

Numerical Technique

Maxwell's equations in the preceding form are solved by an adaptation to the CEM framework of the ENO[5,6] scheme originally developed to solve time-dependent, inviscid compressible fluid flow, given by the Euler equations of gasdynamics that constitute a system of hyperbolic conservation laws.

ENO schemes belong to the class of high-resolution numerical schemes developed to deal with flowfields containing shock waves. They are able to maintain high-order accuracy in smooth regions of the flow, as well as to provide for nonoscillatory shocks. The ENO scheme is able to achieve this dual capacity by employment of an adaptive stenciling procedure. The adaptive stenciling attempts to make use of the smoothest possible information in the computation of the numerical fluxes at the cell interfaces. The points in the stencil that contribute to the computation of numerical fluxes at cell interfaces for the next time step are chosen in a nonlinear manner and depend on the instantaneous solution. The ENO scheme used here is the ENO–Roe form,[9,10] which is an efficient implementation of the original ENO methodology and has the ENO construction procedure based on the numerical fluxes rather than on cell averages of the state variables.

Consider the one-dimension scalar hyperbolic conservation law

$$u_t + f(u)_x = 0 \tag{11}$$

being solved on an uniform grid. The numerical flux at the right-hand face of cell j with the rth-order ENO scheme is

$$\bar{f}_{j+\frac{1}{2}} = \sum_{l=0}^{r-1} \alpha_{k,l}^{r} f_{j-r+1+k+l} \tag{12}$$

where $\alpha_{k,l}^{r}$ are the reconstruction coefficients and k is the stencil index selected among the r candidate stencils, $k = 0, 1, \ldots, r-1$. The stencil S_k can be written as

$$S_k = (x_{j+k-r+1}, x_{j+k-r+2}, \ldots, x_{j+k}) \tag{13}$$

and is locally the smoothest possible stencil.[10] This is applied to the three-dimensional system of Eq. (9) when the system is decoupled into six scalar hyperbolic conservation laws normal to the cell faces.

Scattered Formulation

Equation (9) can be rewritten in operator form

$$\mathcal{L}(\boldsymbol{u}) = \boldsymbol{s} \tag{14}$$

Through decomposition of the total field into incident and scattered fields, Eq. (14) is written as

$$\mathcal{L}(\boldsymbol{u}^i + \boldsymbol{u}^s) = \boldsymbol{s}^i + \boldsymbol{s}^s \tag{15}$$

For the linear system being solved here, this is written as

$$\mathcal{L}(\boldsymbol{u}^s) = \boldsymbol{s}^s - \mathcal{L}(\boldsymbol{u}^i) + \boldsymbol{s}^i \tag{16}$$

or as

$$\mathcal{L}(\boldsymbol{u}^s) = \boldsymbol{s}^s + \boldsymbol{S}^i \tag{17}$$

with

$$\boldsymbol{S}^i = -\mathcal{L}(\boldsymbol{u}^i) + \boldsymbol{s}^i \tag{18}$$

In the scattered field formulation employed here, Eq. (17) is solved in the whole computational domain consisting of freespace and the dielectric layer. If the incident field is taken to be a solution of Maxwell's equations in freespace, then in the absence of $\boldsymbol{J}_i$, the impressed current density vector, the incident field source term $\boldsymbol{S}^i$, is always zero in freespace. Similarly the scattered field source term $\boldsymbol{s}^s$ is also zero in freespace. Thus, as required, the preceding scattered field formulation naturally satisfies

$$\mathcal{L}(\boldsymbol{u}^s) = 0 \tag{19}$$

in freespace. Both the incident and scattered field source terms are not zero in the dielectric and depend on the incident and scattered field, respectively. Thus, the solution in the dielectric is driven by the source terms (which are zero in freespace) and no boundary condition needs to be specified at the dielectric–freespace interface. Only the source terms are required to be added to the formulation in freespace represented by Eq. (19) while operations are performed in the dielectric regions.

Numerical Implementation

The system of equations (9) in the conservative form can, thus, be written in a scattered field formulation as

$$\boldsymbol{u}^s_t + \boldsymbol{f}(\boldsymbol{u}^s)_x + \boldsymbol{g}(\boldsymbol{u}^s)_y + \boldsymbol{h}(\boldsymbol{u}^s)_z = \boldsymbol{s}^s + \boldsymbol{S}^i \tag{20}$$

where

$$\boldsymbol{S}^i = -\boldsymbol{u}^i_t - \boldsymbol{f}(\boldsymbol{u}^i)_x - \boldsymbol{g}(\boldsymbol{u}^i)_y - \boldsymbol{h}(\boldsymbol{u}^i)_z + \boldsymbol{s}^i \tag{21}$$

The solution procedure consists of solution of the Maxwell equations in a scattered field formulation inside the dielectric layer and in freespace. Through integration of the differential form of the conservation law represented by Eq. (20) over an arbitrary control volume $\mathcal{V}$

$$\frac{\partial \int_{\mathcal{V}} \boldsymbol{u}^s \, \mathrm{d}\mathcal{V}}{\partial t} + \int_{\mathcal{V}} \nabla \cdot [\boldsymbol{F}(\boldsymbol{u}^s)] \, \mathrm{d}\mathcal{V} = \int_{\mathcal{V}} (\boldsymbol{s}^s + \boldsymbol{s}^i) \, \mathrm{d}\mathcal{V} - \frac{\partial \int_{\mathcal{V}} \boldsymbol{u}^i \, \mathrm{d}\mathcal{V}}{\partial t} - \int_{\mathcal{V}} \nabla \cdot [\boldsymbol{F}(\boldsymbol{u}^i)] \, \mathrm{d}\mathcal{V} \tag{22}$$

and application of the divergence theorem, the integral form of the conservation law is obtained as

$$\frac{\partial \int_{\mathcal{V}} \boldsymbol{u}^s \, \mathrm{d}\mathcal{V}}{\partial t} + \oint_{\mathcal{S}} [\boldsymbol{F}(\boldsymbol{u}^s) + \boldsymbol{F}(\boldsymbol{u}^i)] \cdot \hat{\boldsymbol{n}} \, \mathrm{d}\mathcal{S} = \int_{\mathcal{V}} \left(\boldsymbol{s}^s + \boldsymbol{s}^i - \boldsymbol{u}^i_t\right) \mathrm{d}\mathcal{V} \tag{23}$$

It is then used to formulate the problem within the framework of the finite volume method in the time domain. The three-dimensional domain is discretized into hexahedral cells, and the integral form applied to each cell with the state vector defined at cell centers. The discretized form for the jth cell is

$$\mathcal{V}_j \frac{\mathrm{d}\tilde{\boldsymbol{u}}^s_j}{\mathrm{d}t} + \sum_{m=1}^{M} \left(\{[\boldsymbol{F}(\boldsymbol{u}^s) + \boldsymbol{F}(\boldsymbol{u}^i)] \cdot \hat{\boldsymbol{n}} \mathcal{S}\}_m \right)_j = \mathcal{V}_j \left(\tilde{\boldsymbol{s}}^s_j + \tilde{\boldsymbol{s}}^i_j - \frac{\mathrm{d}\tilde{\boldsymbol{u}}^i_j}{\mathrm{d}t} \right) \tag{24}$$

where $\tilde{\boldsymbol{u}}^s_j$ indicates the volume average of $\boldsymbol{u}^s$ over cell j and $(\{[\boldsymbol{F}(\boldsymbol{u}^s) + \boldsymbol{F}(\boldsymbol{u}^i)] \cdot \hat{\boldsymbol{n}} \mathcal{S}\}_m)_j$ the average flux through face m of cell j.

The ENO scheme in the ENO–Roe form[9,10] is used to calculate the part of the numerical flux function contribution $[\boldsymbol{F}(\boldsymbol{u}^s) \cdot \hat{\boldsymbol{n}}]_{\text{num}}$ from the scattered field in the spatial discretization for the system of equations (24). The incident field contribution to the numerical flux $[\boldsymbol{F}(\boldsymbol{u}^i) \cdot \hat{\boldsymbol{n}}]_{\text{num}}$ is calculated from the analytical value of the incident field at the cell face. The scattered field contribution to the source term $\tilde{\boldsymbol{s}}^s_j$ in Eqs. (24) is obtained from the value of the scattered field at the cell centers at the beginning of the time step. The incident field contribution to the source term $\tilde{\boldsymbol{s}}^i_j$ and $\mathrm{d}\tilde{\boldsymbol{u}}^i_j/\mathrm{d}t$ in Eqs. (24) can be easily obtained analytically from the incident field representing a continuous wave (and a solution of Maxwell's equations in freespace), defined at the cell centers at the beginning and the end of the time step.

There is no boundary condition to be prescribed at the dielectric–freespace interface. At the dielectric–freespace interface, the arithmetic mean of the electric permittivities ε' and magnetic permeabilities μ' on either side of the interface are used to define the eigenvectors used in the characteristic decomposition of the fluxes required in the computation of the numerical flux in the ENO–Roe formulation.[9,10] Advancement in time is through a total variation diminishing Runge–Kutta time integration,[9] and, unless otherwise mentioned, a second-order spatial and temporal accuracy is chosen in this present work. Calculations are performed until the solution reaches a sinusoidal steady state, and the complex field in the frequency domain is computed from the time history of the solution by the use of a Fourier transform.

Boundary Conditions

For the perfectly conducting surface considered, the total tangential electric field $\hat{\boldsymbol{n}} \times \boldsymbol{E} = 0$ on the conducting surface. This condition is implemented in the scattered field formulation at the perfectly conducting surface by the use of ghost cells inside the body of the scatterer. At the surface of the scatterer,

$$\hat{\boldsymbol{n}} \times \boldsymbol{E}^s + \hat{\boldsymbol{n}} \times \boldsymbol{E}^i = 0 \tag{25}$$

Because the incident field is known analytically, the tangential component of the scattered electric field on the surface of the scatterer ($\hat{\boldsymbol{n}} \times \boldsymbol{E}^s$) can be computed. The values for $\hat{\boldsymbol{n}} \times \boldsymbol{E}^s$ for the ghost cells are extrapolated with this computed value of $\hat{\boldsymbol{n}} \times \boldsymbol{E}^s$ on the scattering surface and the cell-centered values for $\hat{\boldsymbol{n}} \times \boldsymbol{E}^s$ above the surface of the scatterer. The normal component of the scattered electric field in the ghost cells are taken identical to that above the scatterer to obtain the complete scattered electric field in the ghost cells. The scattered magnetic field in these ghost cells are similarly calculated by the enforcement of $\hat{\boldsymbol{n}} \cdot \boldsymbol{B} = 0$ on the perfectly conducting surface.

Standard characteristic boundary conditions are implemented at the outer boundary with the scattered field variables taken as zero in the far field. This can be easily implemented at the flux level in the ENO–Roe formulation[9,10] where the ENO construction procedure is applied to the physical fluxes for the scattered field decomposed along characteristics normal to a cell face. This condition is imposed while the numerical flux is calculated for the scattered field along a particular characteristic direction when the value of the characteristic fluxes for the scattered field is set equal to zero for ghost points outside the computational domain. These ghost points represent the far field, and ENO stencils for calculation of the numerical flux contribution from the scattered field near far-field boundaries would require values for the characteristic fluxes at such ghost points.

Numerical Examples

Nonlossy Coating

The case considered is that of a perfect electric conductor (PEC) sphere covered with a nonlossy but discontinuous coating. The electrical size for the PEC sphere is $ka_2 = 2.6858$. The coating is defined by $ka_1 = 3.0$, $\varepsilon' = 3.0$ and 4.0, and $\mu' = 1.0$. The coated sphere is subject to a continuous harmonic incident wave of wave number k and wavelength $\lambda (k = 2\pi/\lambda)$. The coating is divided equally between two permittivities with the illuminated side having $\varepsilon' = 3.0$. For this example, $t/\lambda = 0.05$, where t is the thickness of the coating and $a_1/a_2 = 1.117$ indicates a fairly thin coating. Figure 1 compares

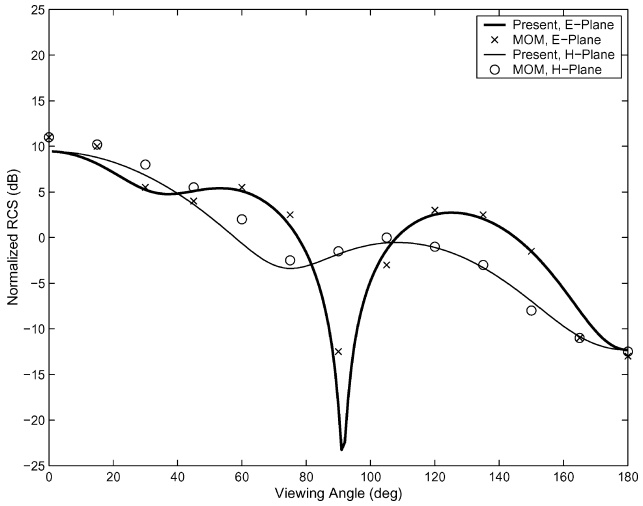

Fig. 1 Bistatic RCS: sphere with discontinuous nonlossy coating, backscatter at 180 deg.

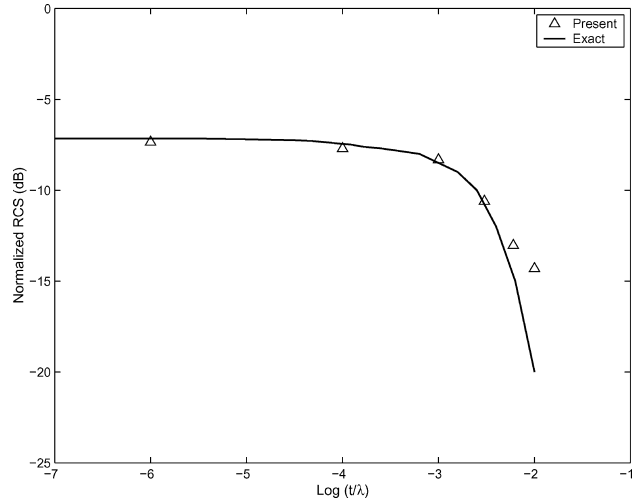

Fig. 2 Monostatic RCS: sphere with lossy coating.

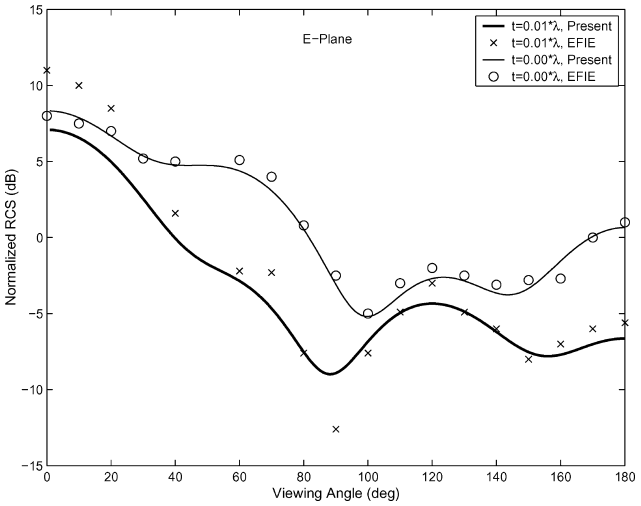

Fig. 3 Bistatic RCS *E*-plane: cone sphere lossy coating, backscatter at 180 deg.

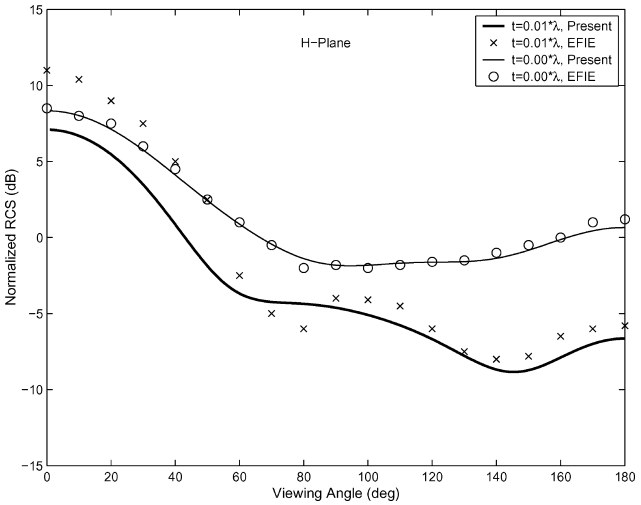

Fig. 4 Bistatic RCS *H*-plane: cone sphere lossy coating, backscatter at 180 deg.

the bistatic radar cross section (RCS) obtained with the present technique and that from method of moments results in Ref. 11. The backscatter point is at a viewing angle of 180 deg. The grid used is an O–O grid with a stretching in the radial direction to cluster the cells close to the boundary of the scatterer. The discretization is 64 points in the azimuthal, 45 in the radial direction, and 32 in the one-half elevation, or a $64 \times 45 \times 32$ grid.

Lossy Coating

The first case considered is of a PEC sphere coated with a dielectric having both electric and magnetic losses. The electrical size for the PEC sphere is $ka_2 = 1.5$. The lossy coating is described by $\varepsilon_r = 3.0 - j4.0$ ($\varepsilon' = 3.0$ and electrical loss tangent $= 4.0/3.0$) and $\mu_r = 5.0 - j6.0$. Calculations were performed in the region from $t/\lambda = 10^{-6}$ to $t/\lambda = 10^{-2}$, and a constant discretization corresponding to $64 \times 48 \times 32$ is used irrespective of the coating thickness. Figure 2 shows variation of backscatter RCS with $\log t/\lambda$ obtained from present computations. This is compared with the exact solution. The agreements tend to be good, especially at relatively lower values of t/λ.

The second case is of a PEC cone–sphere with vertex angle 90 deg and sphere diameter 0.955λ. It is covered with a lossy dielectric with exactly the same permittivity and permeability as in the preceding case. An O–O grid is generated around the cone–sphere first by generation of the grid in the elevation plane and then rotation of the planar grid through 360 deg around the azimuthal. The discretization is $80 \times 40 \times 38$. The cone–sphere is illuminated with a plane wave incident at the cone tip, that is, at a viewing angle of 180 deg (the backscatter point). Bistatic RCS for a coating $t/\lambda = 0.01$ is evaluated with the present technique, and the results compared with that in Ref. 8 obtained by solution of the integral equations in the frequency domain. Exact solutions are not available for this case. Figures 3 and 4 show a comparison of bistatic RCS in the E plane and H plane for $t = 0$ and $t/\lambda = 0.01$. The bistatic plots are in close agreement at the important monostatic, or backscatter, point, where there is a significant reduction in RCS due to the lossy dielectric coating. However, the agreement tends not to be as close around the shadow region (viewing angle of 0 deg) for the coated case.

Test for Numerical Accuracy

Tests for numerical accuracy are performed for the case of the PEC sphere with a lossy coating described earlier. The numerical results obtained are compared with exact values.

The first test concerns order of accuracy, and solutions are obtained with the ENO–Roe scheme of first-, second-, and third-order spatial accuracy on a fixed discretization of $64 \times 48 \times 32$. The first-order ENO–Roe scheme is equivalent to a first-order upwind scheme. Figure 5 shows a comparison of the variation of backscatter RCS with $\log t/\lambda$ for first-, second-, and third-order-accurate results with exact values. Results obtained from higher-order accurate schemes are consistently much closer to exact values compared

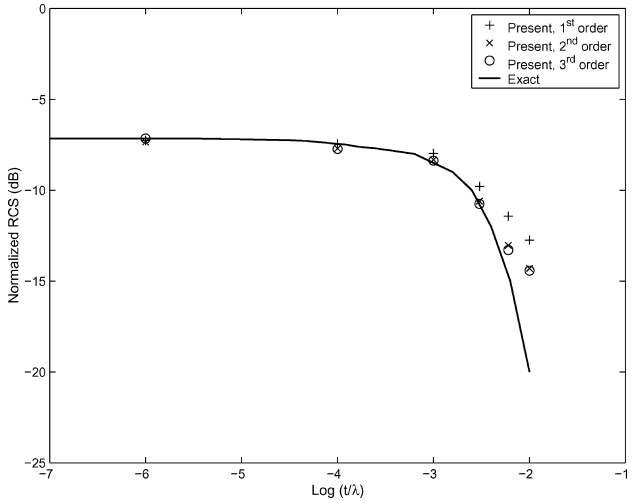

Fig. 5 Monostatic RCS of sphere with lossy coating computed with different orders of accuracy.

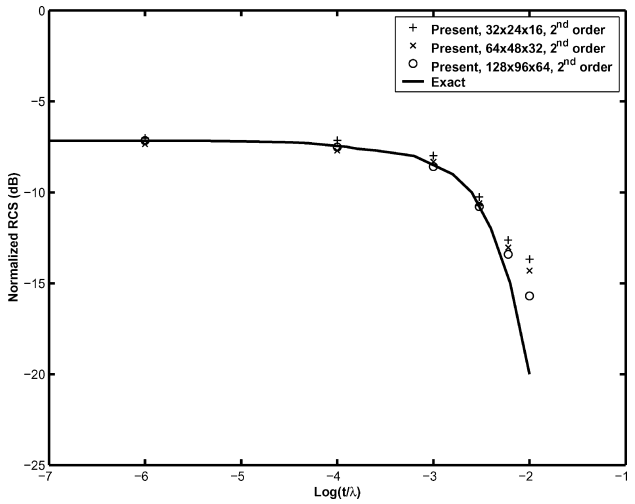

Fig. 6 Monostatic RCS of sphere with lossy coating computed for different discretizations.

to that obtained from the first-order accurate scheme, especially as the thickness of the coating increases. Results obtained with the third-order accurate scheme are relatively closer to exact values compared to that from the second-order-accurate scheme, although this increase in accuracy is relatively less significant compared to the increase in computational time incurred. This is an important issue at large electrical sizes.

In the second test, results are obtained on three different discretizations while the order of accuracy is kept constant. The spatially second-order-accurate scheme is used on discretizations corresponding to $32 \times 24 \times 16$, $64 \times 48 \times 32$, and $128 \times 96 \times 64$. The discretization in the azimuthal and one-half elevation directions result in a uniform grid on the surface of the PEC body in all three cases. In this O–O-type discretization, the average resolution in the dielectric layer, with account taken of the properties of the medium are 5.5, 11.0, and 22.0 cells per wavelength in the azimuthal and one-half elevation directions in the three discretization levels $32 \times 24 \times 16$, $64 \times 48 \times 32$, and $128 \times 96 \times 64$, respectively. These would correspond to resolutions of 21, 43, and 85 cells per wavelength under freespace conditions, respectively. This average resolution was maintained for the respective discretization levels irrespective of the thickness of the dielectric layer being solved for. Because the thickness of the dielectric layer is much less than a wavelength ($t/\lambda = 10^{-6}$–10^{-2}), clustering of cells in the radial or normal direction, including these in the dielectric layer, was used to resolve the dielectric layer for computations. The grid was constant at each discretization level irrespective of the thickness of the dielectric layer being solved for. Thus, more cells are naturally added to the dielectric layer as the thickness of the layer increases. The number of cells in the dielectric layer ranged from 2 at the lowest value of t/λ computed to 10 at the highest value of t/λ computed. Figure 6 compares results for the three different discretizations with exact values. The computed values are again consistently closer to exact values as the grid is refined, especially at higher values of t/λ.

Summary

A characteristic-based FVTD technique based on the ENO methodology is used to solve the Maxwell's equation in the time domain for electromagnetic scattering from perfect conductors coated with a thin layer of nonlossy or lossy dielectric coating. The solution is in the context of a direct formulation where Maxwell's equations are solved in freespace and in the dielectric layer in an unified framework. Numerical examples involving lossy and nonlossy dielectrics show good results for very thin coatings. There is theoretically no restriction in shapes or quality of the dielectric that can be considered. This formulation is an attractive proposition for consideration of very thin dielectric layers that might be problematic in some other formulations, as well as relevant when RAM-coated bodies are considered, especially at lower electrical sizes. Finer discretization is required inside the dielectric layer compared to that prevailing in freespace, leading to increased computational costs. For thicker dielectric layers, this formulation may not be a good choice because the computational costs involved in resolving the dielectric layer adds to the already large computational resource requirement for FVTD techniques.

References

[1]Shankar, V., "A Gigaflop Performance Algorithm for Solving Maxwell's Equations of Electromagnetics," AIAA Paper 91-1578, June 1991.

[2]Shang, J. S., "Characteristic-Based Algorithms for Solving the Maxwell Equations in the Time Domain," *IEEE Antennas and Propagation Magazine*, Vol. 37, No. 3, 1995, pp. 15–25.

[3]Ahuja, V., and Long, L. N., "A Parallel Finite-Volume Runge–Kutta Algorithm for Electromagnetic Scattering," *Journal of Computational Physics*, Vol. 137, No. 2, 1997, pp. 299–320.

[4]Chatterjee, A., and Koruthu, S. P., "Characteristic Based FVTD Scheme for Predicting Electromagnetic Scattering from Aerospace Configurations," *Journal of the Aeronautical Society of India*, Vol. 52, No. 3, 2000, pp. 195–205.

[5]Harten, A., and Osher, S., "Uniformly High-Order Accurate Non-Oscillatory Schemes I," *SIAM Journal on Numerical Analysis*, Vol. 24, No. 2, 1987, pp. 279–309.

[6]Harten, A., Engquist, B., Osher, S., and Chakravarthy, S., "Uniformly High-Order Accurate Essentially Non-Oscillatory Schemes III," *Journal of Computational Physics*, Vol. 71, No. 2, 1987, pp. 231–303.

[7]Shu, C. W., "Preface to the Republication of Uniformly High Order Essentially Non-Oscillatory Schemes, III, by Harten, Engquist, Osher, and Chakravarthy," *Journal of Computational Physics*, Vol. 131, No. 1, 1997, pp. 1–2.

[8]Kishk, A. A., Glisson, A. W., and Goggans, P. M., "Scattering from Conductors Coated with Materials of Arbitrary Thickness," *IEEE Transactions on Antennas and Propagation*, Vol. 40, No. 1, 1992, pp. 108–112.

[9]Shu, C. W., and Osher, S., "Efficient Implementation of Essentially Non-Oscillatory Shock-Capturing Schemes," *Journal of Computational Physics*, Vol. 77, No. 2, 1988, pp. 439–471.

[10]Shu, C. W., and Osher, S., "Efficient Implementation of Essentially Non-Oscillatory Shock-Capturing Schemes II," *Journal of Computational Physics*, Vol. 83, No. 1, 1989, pp. 32–78.

[11]Medgyesi-Mitschangl, L. N., and Putnam, J. M., "Electromagnetic Scattering from Axially Inhomogeneous Bodies of Revolution," *IEEE Transactions on Antennas and Propagation*, Vol. 32, No. 8, 1984, pp. 797–806.

R. Lucht
Associate Editor